Supporting Information

Description of fitting density for crossover helix: The crystal structure of wild-type was solved and the initial placement of the cross over helix residues was challenging. While density of W296 and M297 were apparent, the helical twist was difficult to model. Crystal structure of the high resolution loop truncated structure allowed for the determination of the helicity and the kinking of the cross over helix by P292. The model of the cross over helix built at this resolution was then used to build the cross over helix in the wild-type at low resolution and confirm the positions of the residues and their side chains.

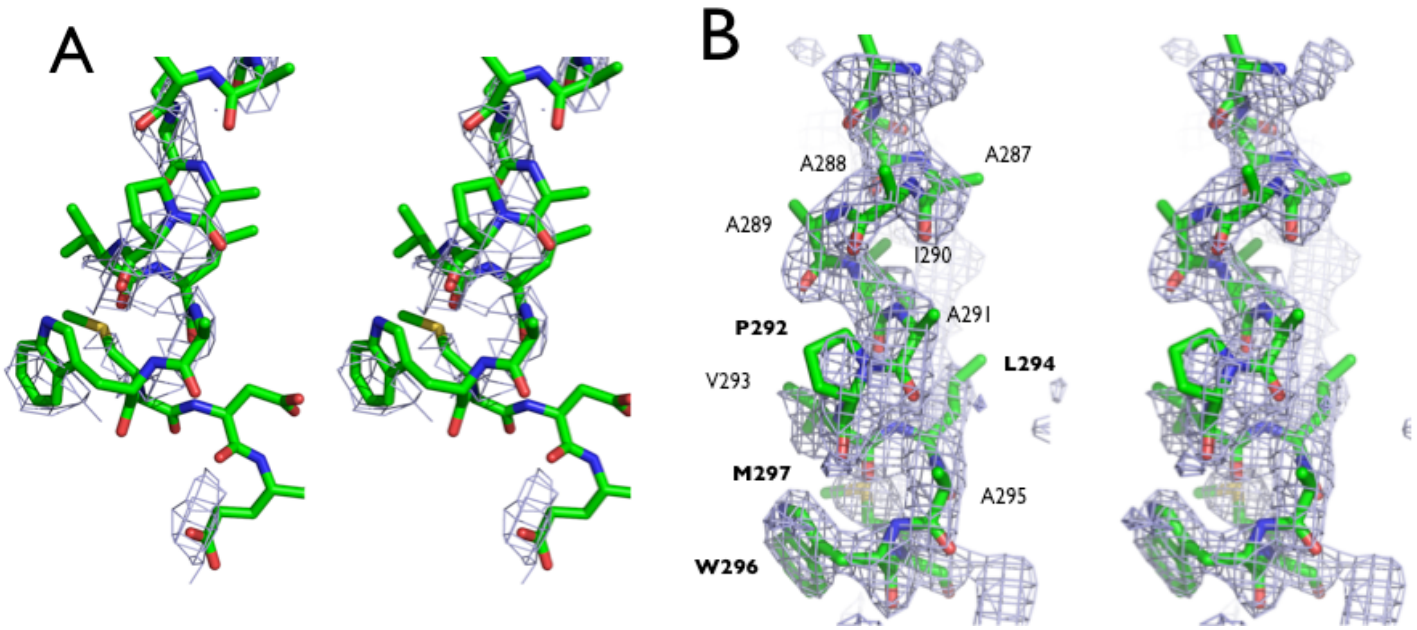

Supplementary Figure 1: Stereo figure of a sim omit difference map (F_o-F_c) contoured at 2.5σ (**A**) and 3σ (**B**) of the crossover helix. Wild-type at 3.7Å (**A**) and loop truncated at 2.2Å (**B**).The helix is shown in green sticks. For molecular replacement, coordinates of the crossover helix and the linker were not included in the search model in order to prevent phase bias in this region. One three cycle run of simulated annealing (starting and final temperature 2500K and 300K, respectively, and 500 cooling steps) and real space refinement was done in Phenix prior to model building in this area. Strong electron (and at high resolution planar) density corresponding to W296 and M297 is clearly present at high and low resolution. If L294, potentially the only other bulky residue of the crossover helix, is placed at W296 density for initial model building, the strong electron density currently observed for M297 could not account for A295, the next amino acid in the sequence, that would be placed there upon the register change. Likewise, P292 would not fit in the electron density for L294 at high resolution. Crystal structures of the *C. hominis* and *P. falciparum* TS-DHFR both contain an aromatic residue at this position of the crossover helix, and thus provide additional support that W296 is placed correctly in the crystal structures presented here. Finally, rich electron density of key side chains at low resolution support that the cross over helix is at the same position when compared wild-type and loop truncated crystal structures.

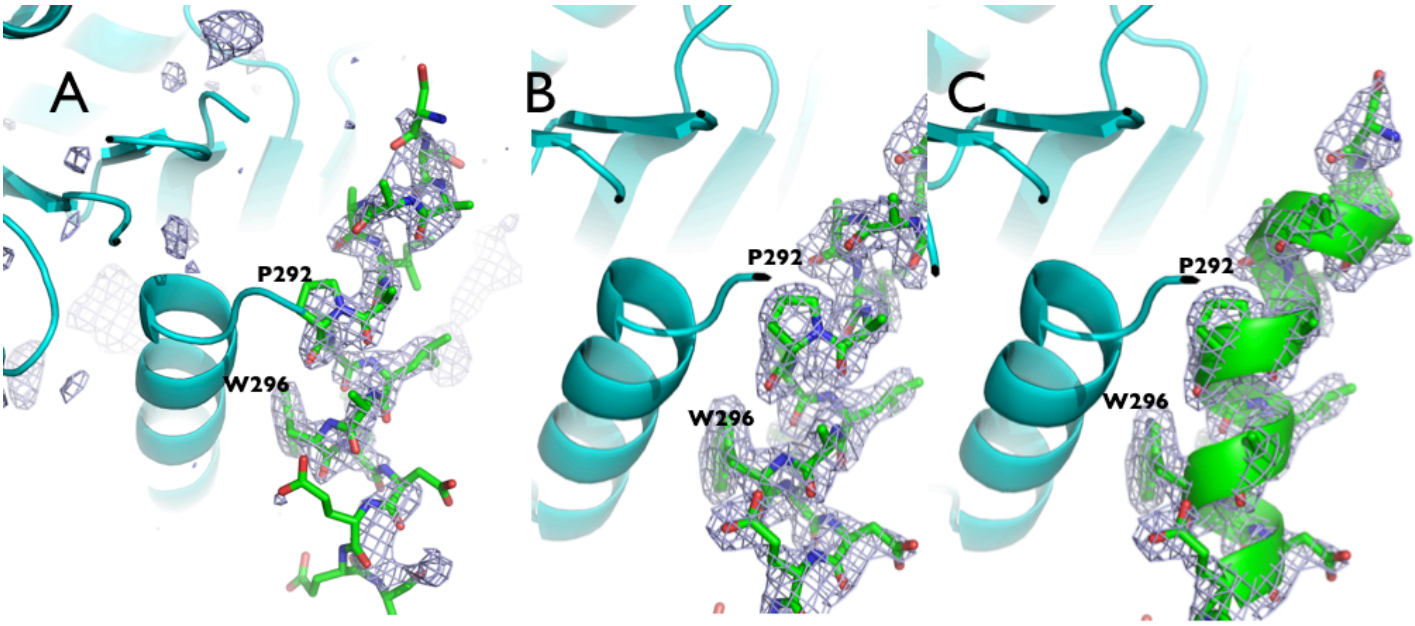

Supplementary Figure 2. A) Sim omit F_o-F_c difference density map of the crossover helix of the loop truncated mutant at 2.2Å resolution, contoured at 3σ. **B**) and **C**) Final $2F_o$-F_c map contoured at 1.5σ. Residues are shown as sticks, and W296 and P292 are labeled. Bending or the kinking of the crossover helix at this resolution can clearly be seen when the helix is shown in cartoon representation (Panel **C**).

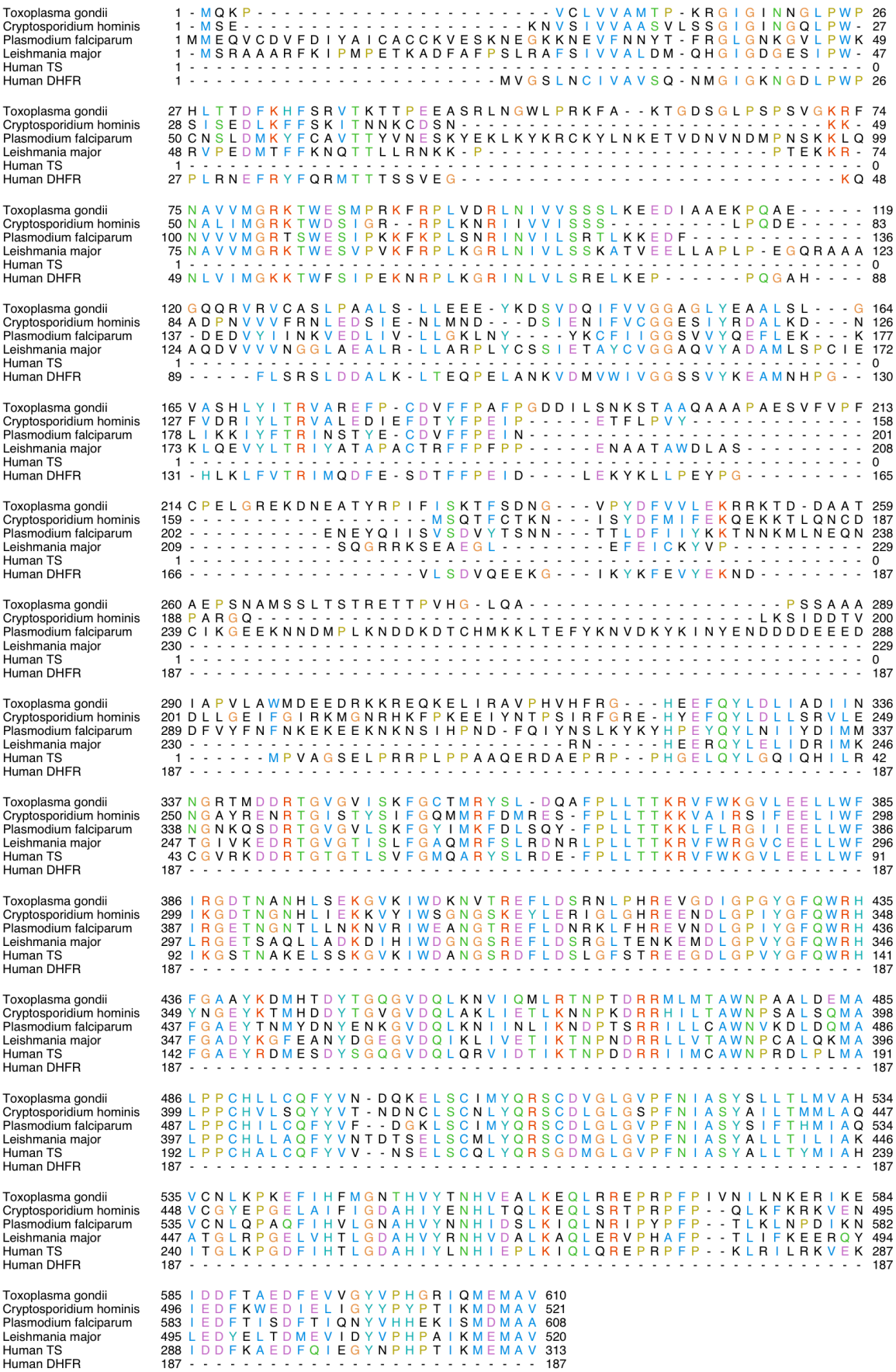

Supplementary Figure 3: Alignment of thymidylate synthase-dihydrofolate reductases. Sequences of bifunctional TS-DHFRs from *T. gondii, C. hominis, P. falciparum,* and *L. major* (GenBank™ accession

Q07422**,** Q5CGA3**,** P13922, and P07382, respectively) and monofunctional human TS and DHFR (accession P04818.3 and AAH71996.1, respectively). The alignment was generated using the COBALT alignment software[(1)] and conserved residues were colored according to the ClustalX color scheme (W,L,V,I,M,F,A,C: *blue*; T,S,N,Q: *green*; G: *orange*; H,Y: *cyan*; P: *yellow*; K,R: *red*; D,E: *magenta*)[(2)].

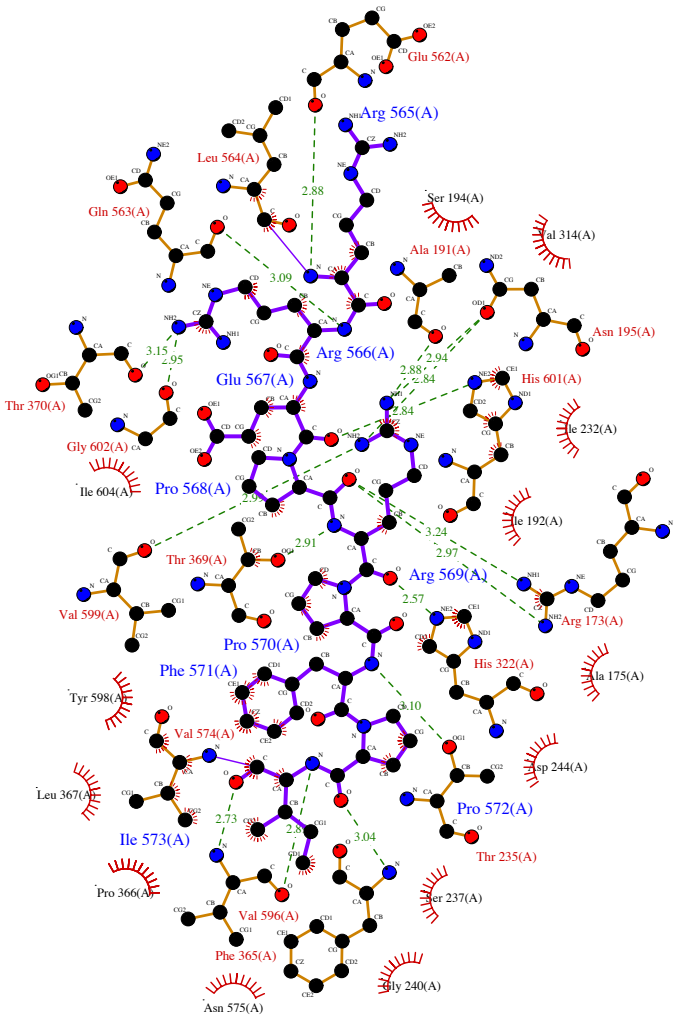

Supplemental Figure 4: Interface between TS and DHFR domains showing that both hydrophobic interactions and salt bridges are prominent between the two domains. Hydrophobic interactions are predominant.

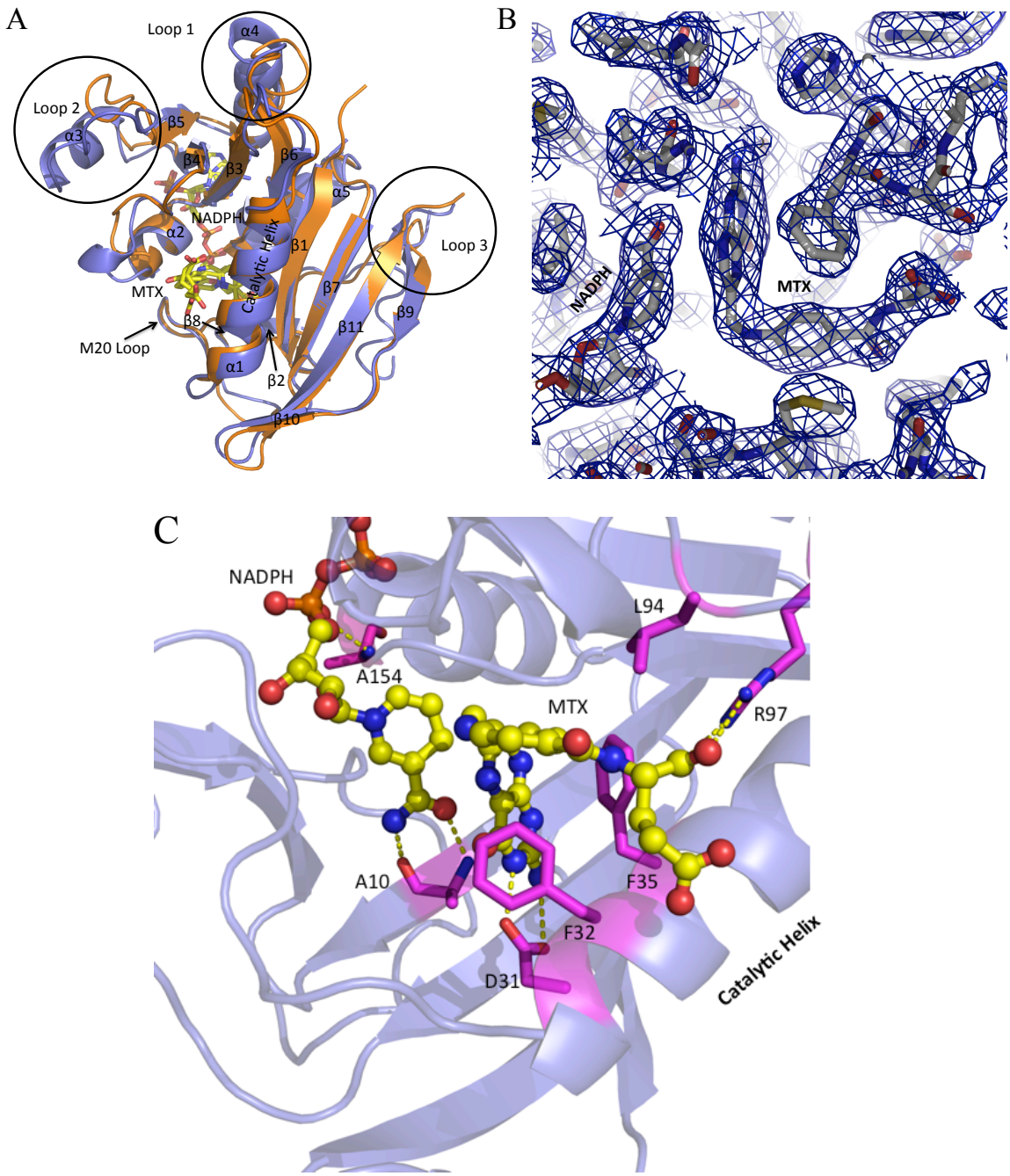

Supplementary Figure 5: Key features of the DHFR domain. (**A**) Superposition of *T. gondii* (blue) and *C. hominis* (orange) DHFR domain. Location of distinct surface loops in *T. gondii* DHFR are shown as indicated. (**B**) Final 2Fo-Fc map, contoured at 1.5 σ , showing the electron density of DHFR active site with ligands NADPH and MTX at 2.2 Å resolution. The ligands were excluded during initial molecular replacement and added in later rounds of refinement. (**C**) Key interactions between the active site ligands and the DHFR domain are shown in magenta.

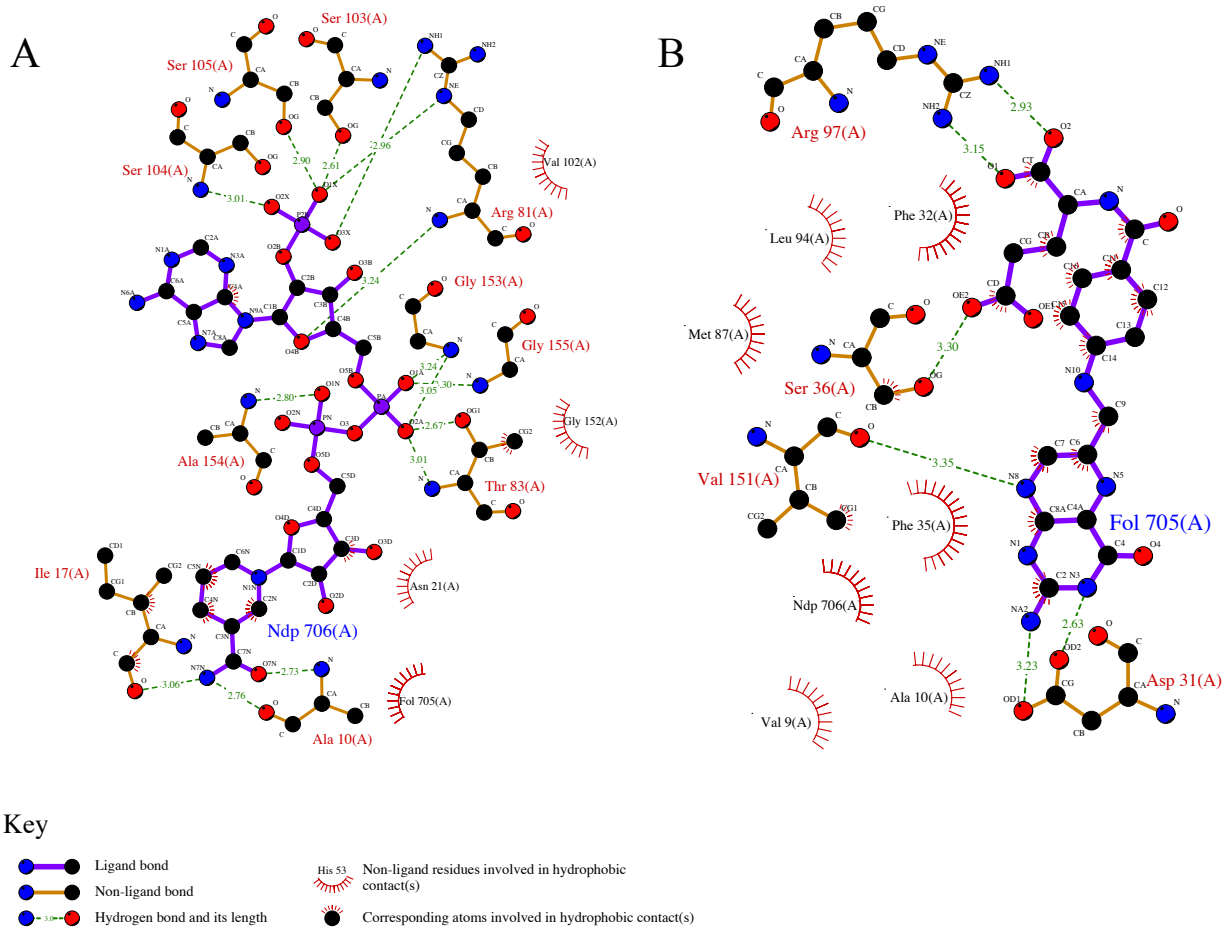

Supplementary Figure 6: Ligand plot illustrating DHFR domain protein-ligand interactions with active site ligands. (**A**) NADPH and (**B**) Methotrexate.

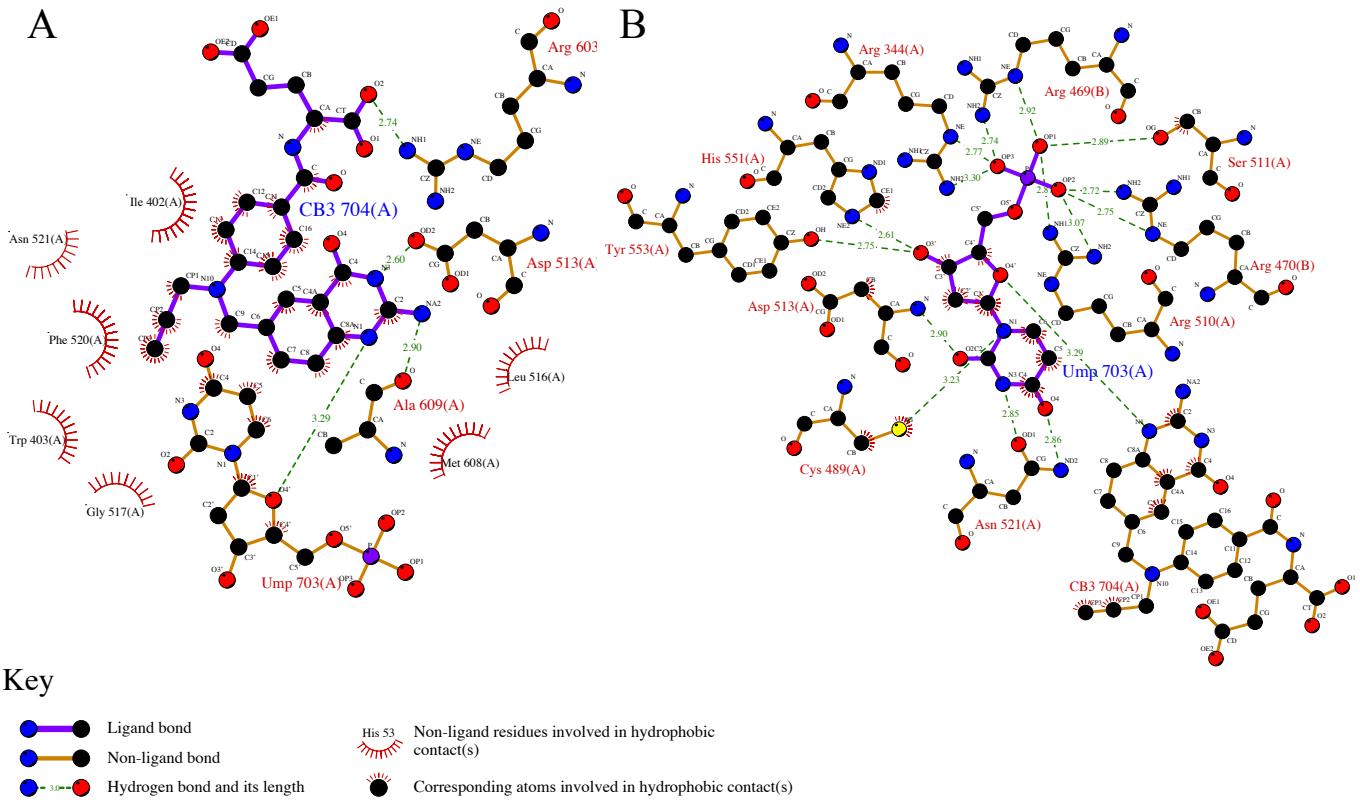

Supplementary Figure 7: Ligand plot illustrating TS domain protein-ligand interactions with active site ligands. (**A**) PDDF (CB3) and (**B**) dUMP.

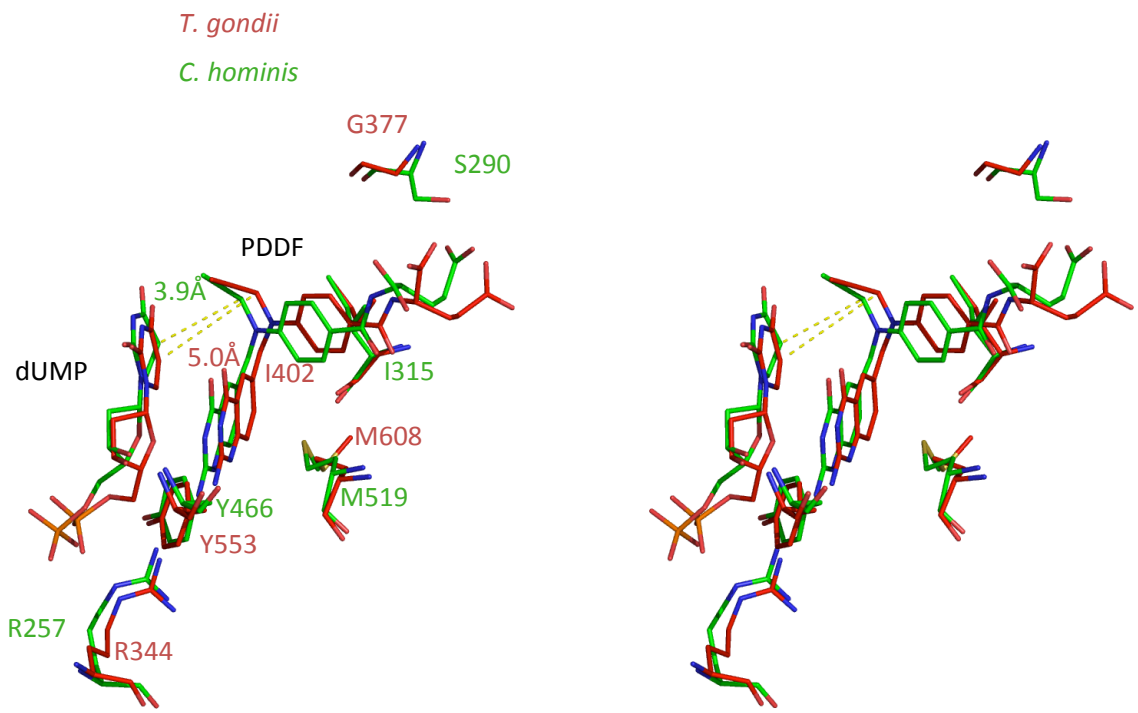

Supplementary Figure 8: Stereo figure of superposition of *T. gondii* and *C. hominis* TS active site. *T. gondii* active site ligands dUMP and PDDF are colored red and *C. hominis* green. Also shown are important residues interacting with the substrates. Note that for the atoms involved in methyl transfer, C5 of dUMP and CP1 of PDDF, the distance for Tg is >1 Å relative to Ch.

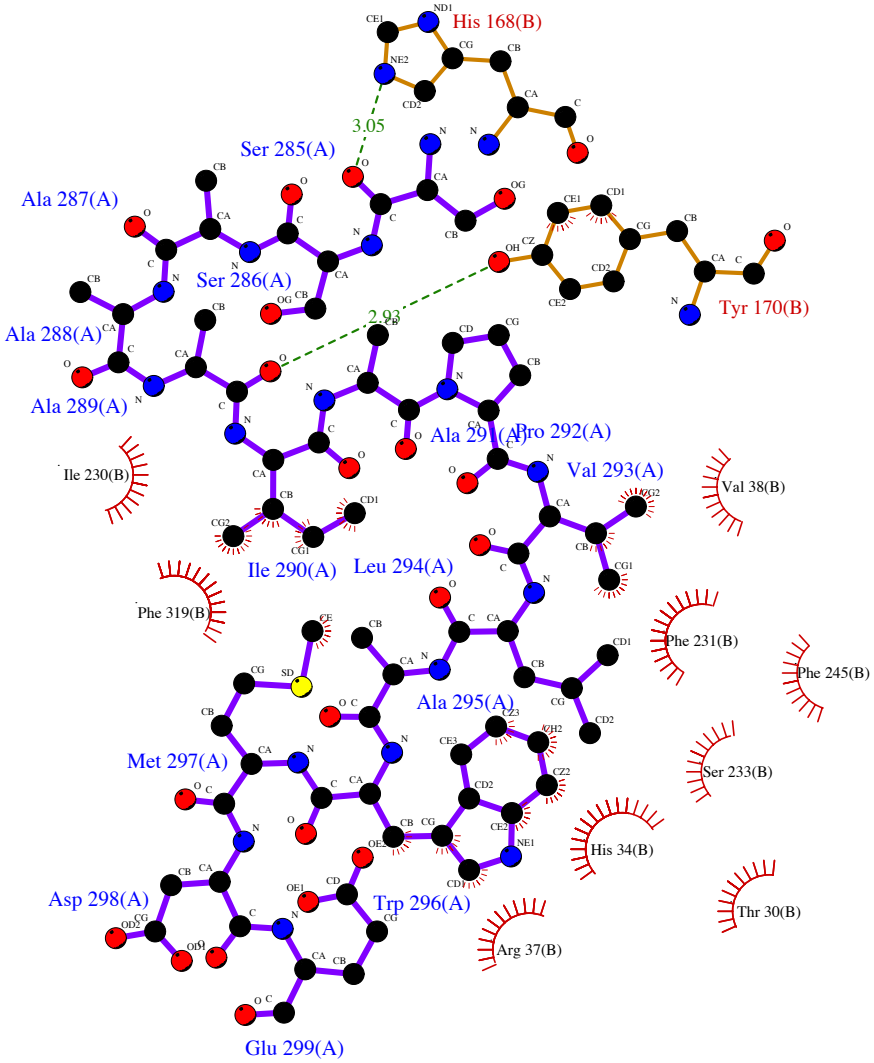

Key

Ligand bond

Non-ligand bond

Hydrogen bond and its length

His 53 Non-ligand residues involved in hydrophobic contact(s)

Corresponding atoms involved in hydrophobic contact(s)

Supplementary Figure 9: Ligand plot illustrating the interface interactions between crossover helix (Residues 285-299) and B-helix are mainly aliphatic. The loop truncated structure was used.

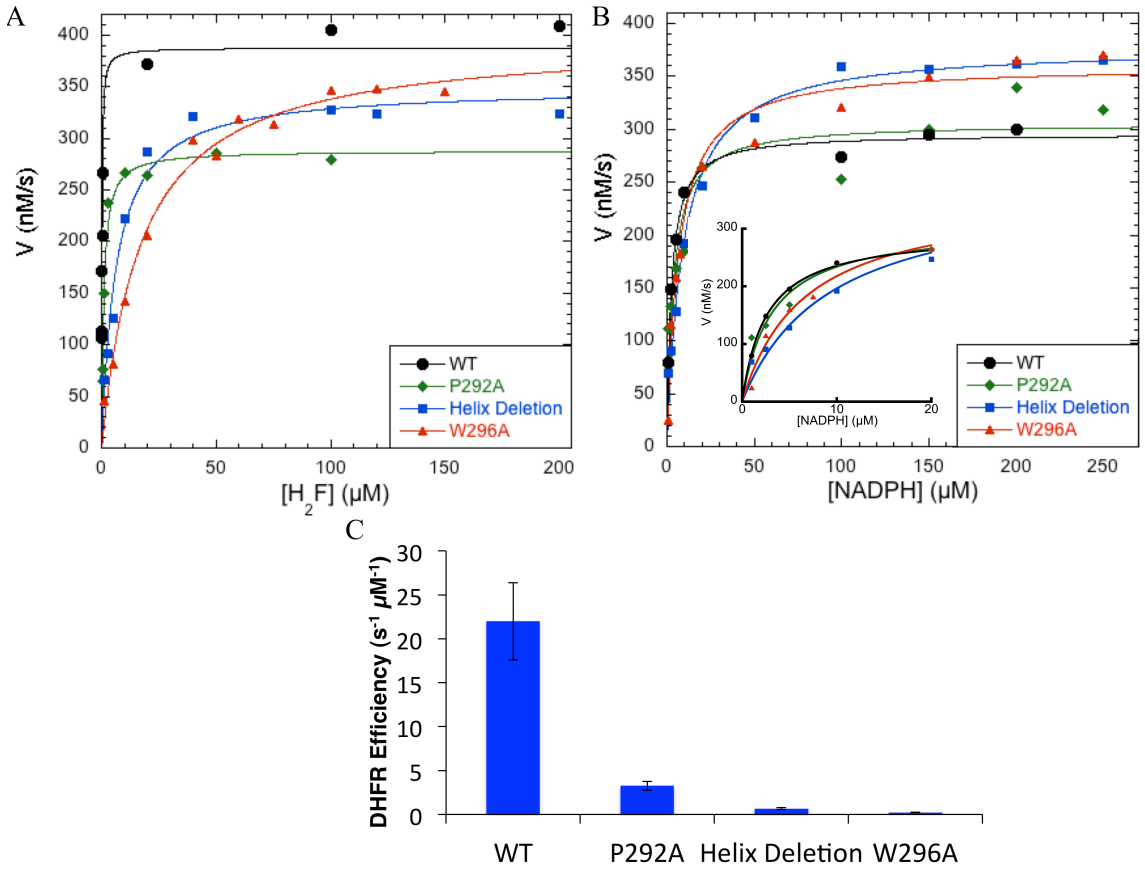

Supplementary Figure 10: Effect of crossover helix mutations on DHFR steady state reaction. Rate constants for steady state experiments were estimated by fitting the data to a Michaelis-Menten hyperbolic curve ($v = V_{max}[S]/(K_m+[S])$ using Kaleidagraph. Enzyme efficiencies were calculated using the equation $Efficiency = k_{cat}/K_m$. (**A**) Effect of crossover helix mutants on steady state H_2F binding. (**B**) Effect of crossover helix mutants on steady state NADPH binding (Inset: steady state rate plot at lower concentrations of NADPH). Individual data points are the average of experiments repeated in duplicate or triplicate and variance does not exceed 10% for any point included. (**C**) Efficiency of WT *T. gondii* DHFR compared to crossover helix mutants. Efficiency was calculated using the K_m of H_2F and k_{cat} of the DHFR reaction in each case. Errors in k_{cat}, K_m, and efficiency result from standard error of parameters.

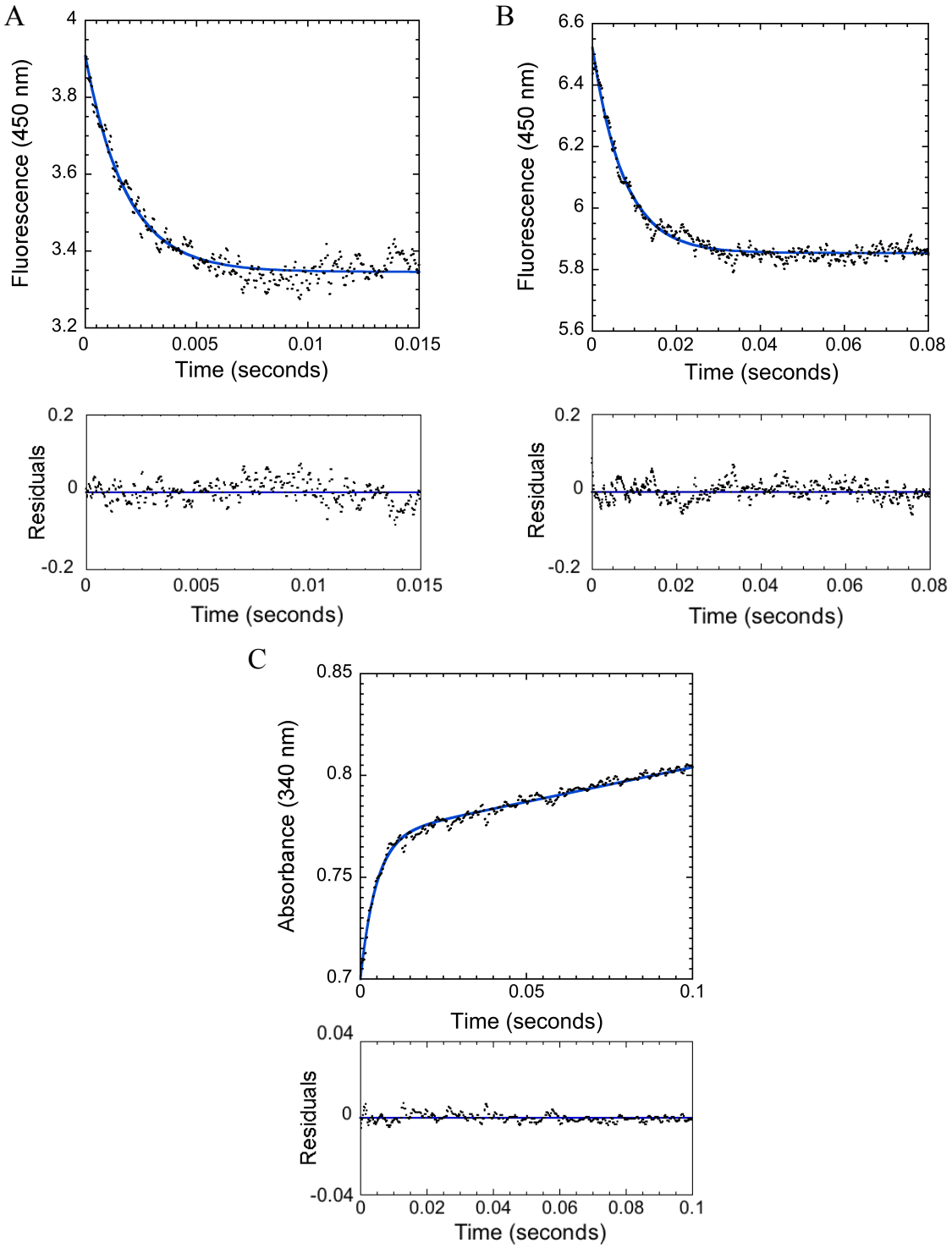

Supplementary Figure 11: Representative stopped-flow fluorescence traces of DHFR and TS catalysis. Each trace is an average of three replicates. Residuals are shown below each plot. (**A-B**) For the DHFR reaction, 50 µM enzyme was incubated with 250 µM NADPH and mixed with 25 µM H_2F. Coenzyme fluorescence energy transfer was measured using an output filter at 450 nm (± 10 nm) and the resultant data were fit in Kaleidagraph to a single exponential curve, *Fluorescence* = $Ae^{(-kchem*time)}$. Shown are the traces for the (**A**) P292A and (**B**)

helix deletion mutants. (**C**) Representative stopped-flow absorbance trace of the TS burst reaction for the wild-type enzyme. 25 μM enzyme was incubated with 1 mM dUMP and mixed with 500 μM CH_2H_4F and absorbance was measured with an output filter at 340 nm (± 10 nm). The trace was fit to a burst curve $Fluorescence = Ae^{(-kburst*time)} + k_{ss}*time$.

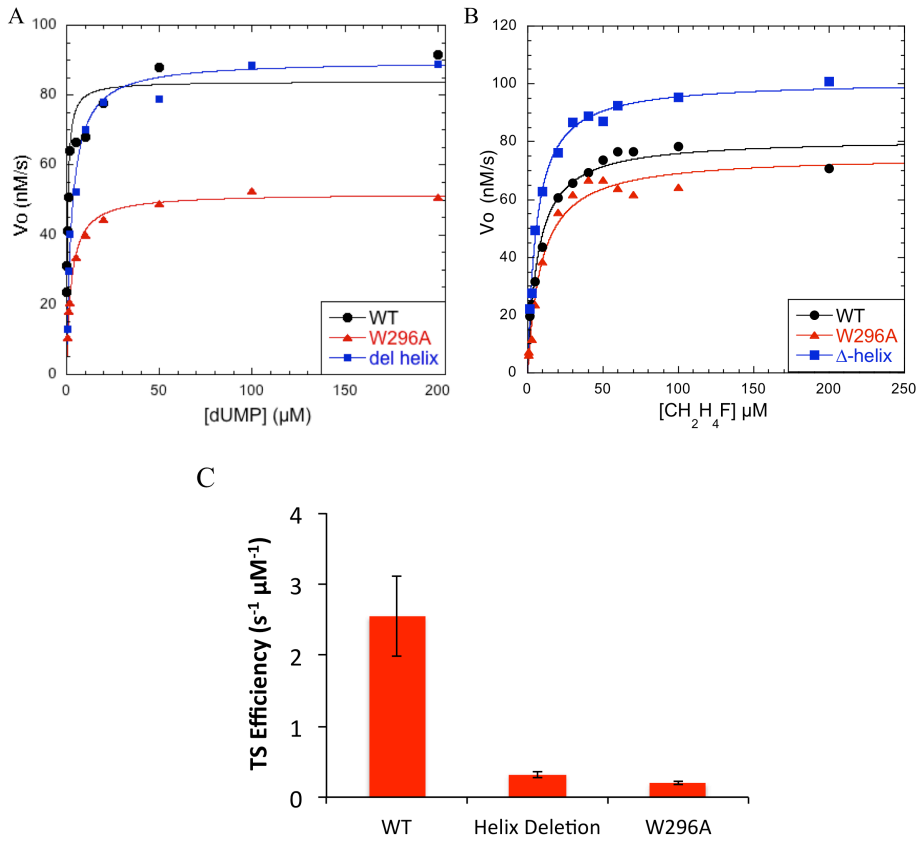

Supplementary Figure 12: Effect of crossover helix mutations on TS steady state reaction. Rate constants for steady state experiments were estimated by fitting the data to a Michaelis-Menten hyperbolic curve ($v = V_{max}[S]/(K_m+[S])$ using Kaleidagraph. Enzyme efficiencies were calculated using the equation $Efficiency = k_{cat}/K_m$. (**A**) Effect of crossover helix mutants on steady state dUMP binding. (**B**) Effect of crossover helix mutants on steady state CH_2H_4F binding. Individual data points are the average of experiments repeated in duplicate or triplicate and variance does not exceed 10% for any point included. (**C**) Efficiency of WT *T. gondii* TS compared to crossover helix mutants. Efficiency was calculated using the K_m of dUMP and k_{cat} of the TS reaction in each case. Errors in k_{cat}, K_m, and efficiency result from standard error of parameters.

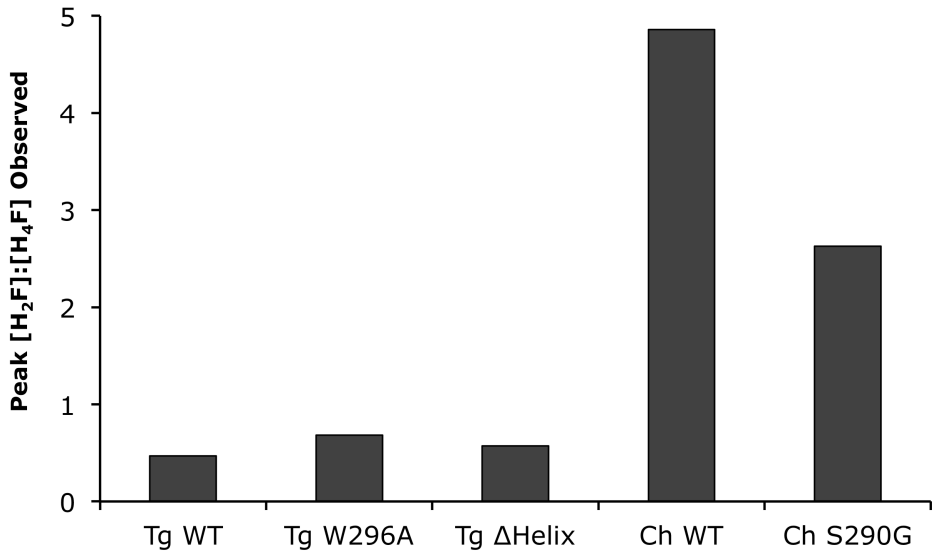

Supplemental Figure 13: Bar graph representing $[H_2F]/[H_4F]$ at peak H_2F concentration during the single turnover bifunctional reaction (*See Figure 4, red arrows*). Enzyme (50 μM) was incubated with dUMP (500 μM), and NADPH (500 μM) and mixed with $[^3H]$-CH_2H_4F (10 μM).

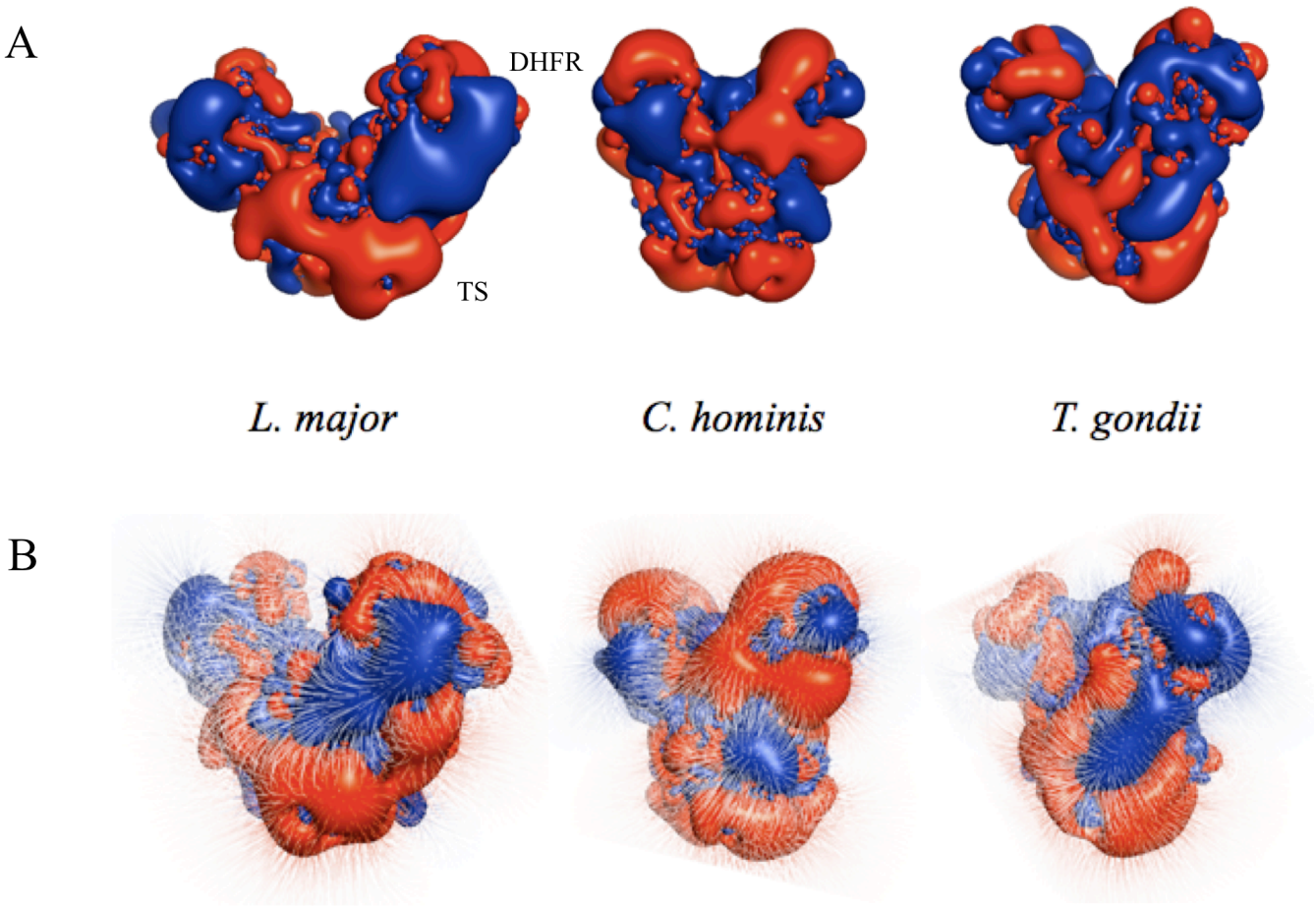

Supplementary Figure 14: (**A**) Poisson-Boltzmann electrostatic surface representation of TS-DHFRs from *L. major* (left), *C. hominis* (middle), and *T. gondii* (right). Electrostatic field greater than 0.5 kT/e is shown in blue, less than -0.5 kT/e is shown in red. (**B**) Electrostatic field lines of *L. major*, *C. hominis*, and *T. gondii* TS-DHFR. The negative field lines suggest that the surface charges of *C. hominis* DHFR may prevent the negatively charged H_2F from channeling. The coloumbic charges were created by using the program Chimera employing default settings. [3] The negative charges are colored red, and positive charges are colored blue.

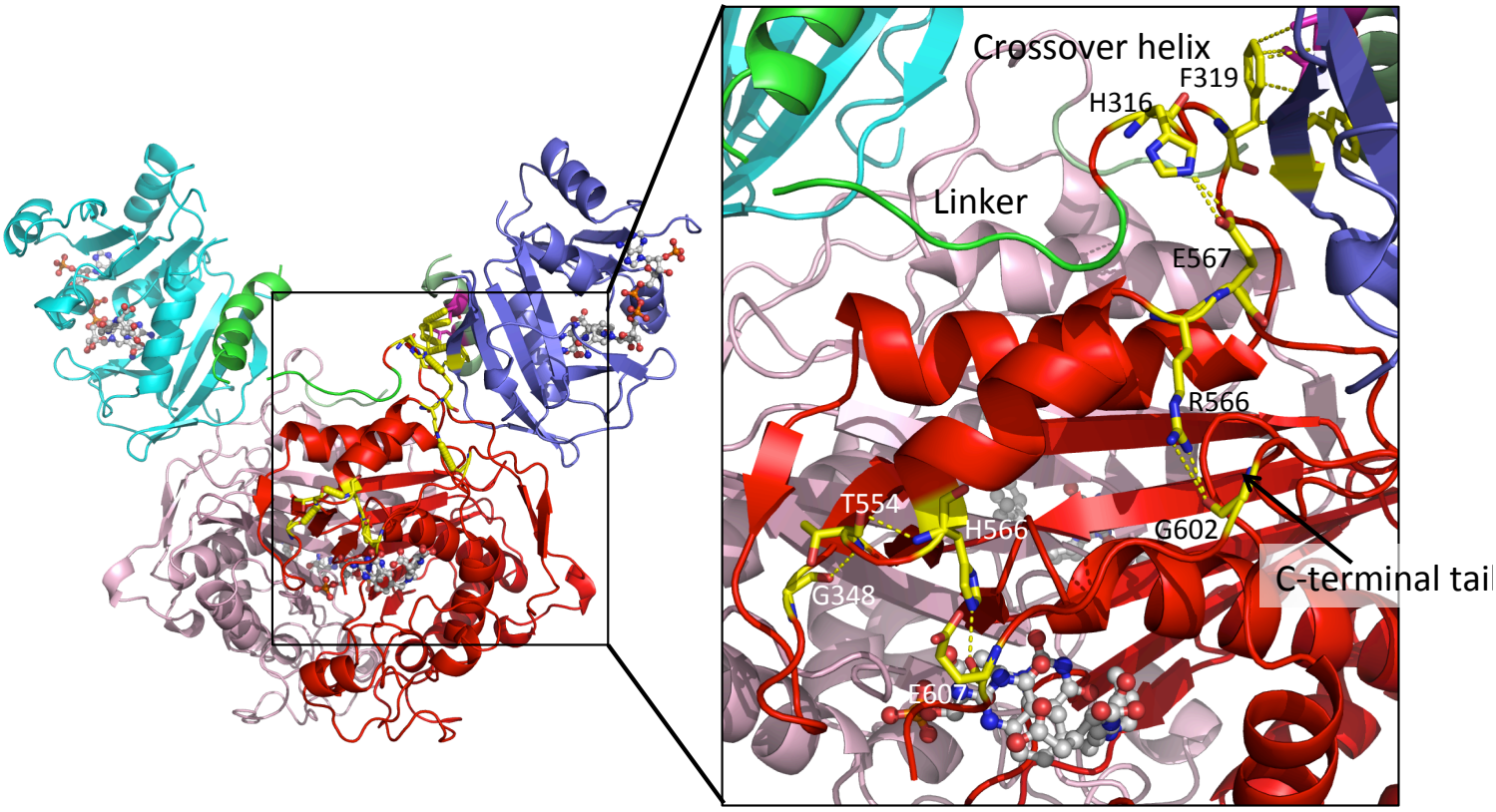

Supplementary Figure 15: Possible mechanism for crossover helix and distal TS allosteric interactions. The domains are colored as described in Figure 2A. Key residues important for allostery are colored in yellow. Salt bridges and hydrogen bonds are shown as yellow dashes.

References

1. Papadopoulos, J. S., and Agarwala, R. (2007) COBALT: constraint-based alignment tool for multiple protein sequences, *Bioinformatics 23*, 1073-1079.
2. Larkin, M. A., Blackshields, G., Brown, N. P., Chenna, R., McGettigan, P. A., McWilliam, H., Valentin, F., Wallace, I. M., Wilm, A., Lopez, R., Thompson, J. D., Gibson, T. J., and Higgins, D. G. (2007) Clustal W and Clustal X version 2.0, *Bioinformatics 23*, 2947-2948.
3. Pettersen, E. F., Goddard, T. D., Huang, C. C., Couch, G. S., Greenblatt, D. M., Meng, E. C., and Ferrin, T. E. (2004) UCSF Chimera--a visualization system for exploratory research and analysis, *Journal of computational chemistry 25*, 1605-1612.